

A HIGHER-ORDER UPWIND METHOD FOR VISCOELASTIC FLOW

Andrew Nonaka, David Trebotich, Gregory H. Miller,
Daniel T. Graves, and Phillip Colella

August 29, 2008

Abstract

We present a conservative finite difference method designed to capture elastic wave propagation in viscoelastic fluids in two dimensions. We model the incompressible Navier-Stokes equations with an extra viscoelastic stress described by the Oldroyd-B constitutive equations. The equations are cast into a hybrid conservation form which is amenable to the use of a second-order Godunov method for the hyperbolic part of the equations, including a new exact Riemann solver. A numerical stress splitting technique provides a well-posed discretization for the entire range of Newtonian and elastic fluids. Incompressibility is enforced through a projection method and a partitioning of variables that suppresses compressive waves. Irregular geometry is treated with an embedded boundary/volume-of-fluid approach. The method is stable for time steps governed by the advective CFL condition. We present second-order convergence results in L^1 for a range of Oldroyd-B fluids.

MSC2000: 65N06, 76D05.

Keywords: Viscoelasticity, Oldroyd-B fluid, Godunov method, Riemann solver, projection method, embedded boundaries

1 Introduction

The governing equations for viscoelastic flow of an Oldroyd-B fluid are the incompressible Navier-Stokes equations plus an extra viscoelastic stress described by the Oldroyd-B constitutive equations:

$$\frac{\partial \mathbf{u}}{\partial t} + (\mathbf{u} \cdot \nabla) \mathbf{u} - \frac{1}{\rho} \nabla \cdot \boldsymbol{\tau} = -\frac{1}{\rho} \nabla p + \frac{\mu_s}{\rho} \Delta \mathbf{u}, \quad (1)$$

$$\nabla \cdot \mathbf{u} = 0, \quad (2)$$

$$\frac{\partial \boldsymbol{\tau}}{\partial t} + (\mathbf{u} \cdot \nabla) \boldsymbol{\tau} - (\nabla \mathbf{u}) \boldsymbol{\tau} - \boldsymbol{\tau} (\nabla \mathbf{u})^T = \frac{\mu_p}{\lambda} 2\mathbf{D} - \frac{1}{\lambda} \boldsymbol{\tau}, \quad (3)$$

where \mathbf{u} is the fluid velocity, $\boldsymbol{\tau}$ is the polymeric stress tensor, p is the isotropic pressure, and $\mathbf{D} = [\nabla \mathbf{u} + (\nabla \mathbf{u})^T]/2$ is the rate-of-strain tensor. The parameters that

describe the fluid are the density, ρ , relaxation time, λ , and the solvent and polymeric contributions to the total viscosity, $\mu = \mu_s + \mu_p$. The dimensionless parameters that characterize these types of flows are the Reynolds number, $\text{Re} = \frac{\rho UL}{\mu}$, and the Weissenberg number, $\text{We} = \frac{\lambda U}{L}$, where U and L are the characteristic velocity and length, respectively.

Though the Reynolds number and the Weissenberg number independently characterize viscoelastic flows, it is the elastic Mach number, $\text{Ma} = \sqrt{\text{Re} \cdot \text{We}}$, that is the critical parameter in determining well-posedness of the system. In particular, the system of equations exhibits a change in type from parabolic to hyperbolic when the elastic Mach number becomes supercritical ($\text{Ma} > 1$), admitting propagation of discontinuities. This mathematical behavior was alluded to in the experimental results of Ultman and Denn [33] and formally noted in [7, 18]. It is primarily for this reason (among other symptoms such as large, unbounded normal stresses) that numerical methods have failed to compute stable and convergent steady-state solutions to viscoelastic flows in the presence of geometric singularities, also known as the “High Weissenberg Number Problem”. In addition, using an analogy to transonic flow where the characteristic velocity transitions to a value greater than the speed of sound, Joseph suggested that a method suitable for transonic flows may be needed for the transition to supercritical viscoelastic flows [17]. The analysis described in [30] capitalized on this concept in the design of a numerical algorithm that resolves unsteady elastic wave behavior in viscoelastic fluids.

In this paper, we extend the previous numerical algorithm [30] by leveraging the conservative hyperbolic formulation described therein to design a suitable to higher resolution upstream method for the hyperbolics. In the original algorithm the Oldroyd-B equation is recast into a well-posed hyperbolic form with source terms using a stress-splitting technique; a Lax-Wendroff method is used to discretize the quasi-linear form of the hyperbolic part in the context of a predictor-corrector projection method. (Projection methods are an approach to enforcing the constraint in incompressible flows [3, 2] and have proven to be successful in treating unsteady viscoelastic flows [19, 30].) Our new method uses a second-order Godunov method [5, 6], instead of Lax-Wendroff as in [30], to discretize the hyperbolic part of the equations, resulting in two immediate advantages. First, the maximum time step is increased by a factor of four to allow an advective CFL number restriction of $0 < \text{CFL} < 1$. Second, we can apply second-order conservative finite volume techniques which have been developed for hyperbolic conservation laws [6], elliptic equations [16], and parabolic equations [22] in an embedded boundary (EB) framework for irregular geometry. Our results are consistent with the modified equation analysis in these methods, and we obtain second-order solution error convergence in L^1 for a range of Oldroyd-B fluids.

2 Hyperbolic Analysis

Through the introduction of the inverse deformation tensor, \mathbf{g} , which links material (Lagrangian) coordinates, \mathbf{X} , and spatial (Eulerian) coordinates, \mathbf{x} , as in:

$$g_{\alpha\beta} = \frac{\partial X_\alpha}{\partial x_\beta}, \quad (4)$$

the advective part of the PDE for viscoelastic stress (3) may be put in conservation form. The quantity \mathbf{M} is conserved:

$$\mathbf{M} \equiv \mathbf{g}(\boldsymbol{\tau} + \rho a^2 \mathbf{I})\mathbf{g}^T, \quad (5)$$

$$\frac{\partial \mathbf{M}}{\partial t} + \nabla \cdot (\mathbf{u} \otimes \mathbf{M}) = \mathbf{g} \left[-\frac{1}{\lambda} \boldsymbol{\tau} + \left(\frac{\mu_p}{\lambda} - \rho a^2 \right) 2\mathbf{D} \right] \mathbf{g}^T, \quad (6)$$

$$\frac{\partial \mathbf{g}\mathbf{e}_d}{\partial t} + \frac{\partial}{\partial x_d} \mathbf{g}\mathbf{u} = [\mathbf{u} \times (\nabla \times \mathbf{g}^T)]^T \mathbf{e}_d. \quad (7)$$

The PDE for \mathbf{g} and its right hand side are described in detail in [23]. Here a is an arbitrary constant with dimensions of velocity. As developed in [30], this fictitious wave speed may be treated as a parameter that affects the partitioning of hyperbolic and elliptic terms. Through proper choice of that parameter, the Courant-Friedrichs-Lewy (CFL) limiting time step of the hyperbolic partition can be improved by several orders of magnitude in the Newtonian limit ($\lambda \rightarrow 0$). Here, for purposes of analysis, a need only satisfy $\min_d(\rho a^2 + \tau_{dd}) > 0$.

All together, the coupled PDEs (1)-(3) may be written in the form:

$$\frac{\partial \mathbf{U}}{\partial t} + \frac{\partial \mathbf{F}_\alpha}{\partial x_\alpha} = \mathbf{S}_h(\mathbf{U}) + \mathbf{S}_i(\mathbf{U}, \nabla \mathbf{U}, \Delta \mathbf{U}), \quad (8)$$

where the left hand side is a system of conservation laws, and the right hand side contains proper hyperbolic source terms, \mathbf{S}_h , and improper (elliptic) source terms, \mathbf{S}_i . \mathbf{U} is the vector of conserved quantities:

$$\mathbf{U} = (\mathbf{u}, \mathbf{M}, \mathbf{g}\mathbf{e}_0, \dots, \mathbf{g}\mathbf{e}_{D-1})^T, \quad (9)$$

$$\mathbf{F}_d = \left(u_d \mathbf{u} - \frac{1}{\rho} \boldsymbol{\tau} \mathbf{e}_d, u_d \mathbf{M}, \mathbf{g}\mathbf{u} \delta_{0d}, \dots, \mathbf{g}\mathbf{u} \delta_{D-1,d} \right)^T, \quad (10)$$

$$\mathbf{S}_h = \left(-\frac{1}{\rho} \nabla p, -\frac{1}{\lambda} \mathbf{g} \boldsymbol{\tau} \mathbf{g}^T, 0, \dots, 0 \right)^T, \quad (11)$$

$$\mathbf{S}_i = \left(\nu_s \Delta \mathbf{u}, 2 \left(\frac{\mu_p}{\lambda} - \rho a^2 \right) \mathbf{g} \mathbf{D} \mathbf{g}^T, \right. \\ \left. [\mathbf{u} \times (\nabla \times \mathbf{g}^T)]^T \mathbf{e}_0, \dots, [\mathbf{u} \times (\nabla \times \mathbf{g}^T)]^T \mathbf{e}_{D-1} \right)^T. \quad (12)$$

We analyze the hyperbolic subsystem in primitive variables, \mathbf{W} . The linearization of (8) in primitive variables gives matrices whose eigenvalues are wave speeds, and whose eigenvectors determine the characteristics. If, in the 1D analysis of these linearized equations for direction d , primitive variable u_d is included, then wave

speeds and characteristics describing compressive wave motion are observed. Yet, omission of u_d and its corresponding stress τ_{dd} is also inaccurate [9] since variation in these quantities is permitted by the multidimensional equations. The approach to this dilemma, after [9, 8] is to block partition the primitive equations, treating dependence on gradients of the variables u_d and τ_{dd} as source terms from the point of view of the remaining variables. We will refer to the variable partition (u_d, τ_{dd}) as “inactive” (subscript I), and the remaining variable partition as “active” (subscript A). For $d = 0$,

$$\mathbf{W}_0^T = \left(\mathbf{W}_{A,0}^T \mid \mathbf{W}_{I,0}^T \right) = \left(u_1, \tau_{10}, \tau_{11}, g_{00}, g_{10}, g_{01}, g_{11} \mid u_0, \tau_{00} \right). \quad (13)$$

The primitive variable τ_{01} is omitted because $\boldsymbol{\tau}$ is symmetric. In these variables, the linearized homogeneous advection equation in direction $d = 0$ is:

$$\frac{\partial \mathbf{W}_0}{\partial t} + \mathbf{A}_0 \frac{\partial \mathbf{W}_0}{\partial x_0} = 0, \quad (14)$$

$$\begin{aligned} \mathbf{A}_0 &= \left[\begin{array}{c|c} \mathbf{A}_{AA,0} & \mathbf{A}_{AI,0} \\ \hline \mathbf{A}_{IA,0} & \mathbf{A}_{II,0} \end{array} \right] \\ &= \left[\begin{array}{cccccc|cc} u_0 & -\frac{1}{\rho} & 0 & 0 & 0 & 0 & 0 & 0 \\ -\rho c_0^2 & u_0 & 0 & 0 & 0 & 0 & -\tau_{10} & 0 \\ -2\tau_{10} & 0 & u_0 & 0 & 0 & 0 & 0 & 0 \\ g_{01} & 0 & 0 & u_0 & 0 & 0 & g_{00} & 0 \\ g_{11} & 0 & 0 & 0 & u_0 & 0 & g_{10} & 0 \\ 0 & 0 & 0 & 0 & 0 & u_0 & 0 & 0 \\ 0 & 0 & 0 & 0 & 0 & 0 & 0 & 0 \\ \hline 0 & 0 & 0 & 0 & 0 & 0 & u_0 & -\frac{1}{\rho} \\ 0 & 0 & 0 & 0 & 0 & 0 & -2\rho c_0^2 & u_0 \end{array} \right], \quad (15) \end{aligned}$$

with $c_d = \sqrt{a^2 + \tau_{dd}/\rho}$. The diagonal matrix of eigenvalues of partition $\mathbf{A}_{AA,0}$ is:

$$\boldsymbol{\Lambda}_0 = \text{diag} (u_0 - c_0, u_0, u_0, u_0, u_0, u_0, u_0 + c_0)^T. \quad (16)$$

The corresponding right eigenvectors are given by the columns of:

$$\mathbf{R}_0 = \left[\begin{array}{cccccc|c} -c_0 & 0 & 0 & 0 & 0 & 0 & c_0 \\ -\rho c_0^2 & 0 & 0 & 0 & 0 & 0 & -\rho c_0^2 \\ -2\tau_{10} & 1 & 0 & 0 & 0 & 0 & -2\tau_{10} \\ g_{01} & 0 & 1 & 0 & 0 & 0 & g_{01} \\ g_{11} & 0 & 0 & 1 & 0 & 0 & g_{11} \\ 0 & 0 & 0 & 0 & 1 & 0 & 0 \\ 0 & 0 & 0 & 0 & 0 & 1 & 0 \end{array} \right]. \quad (17)$$

2.0.1 An Exact Riemann Solver

For the incompressible Euler equations, Bell et al. [2] construct edge-centered time-centered predictor states using Taylor series with upwind derivatives. For those equations, their approach is identical to using a higher-order Godunov predictor because “upwinding” solves exactly the associated Riemann problem. In the present system of equations, the wave structure is more complex, but there are no genuinely nonlinear waves, i.e.,

$$(\nabla_{\mathbf{W}_A} \Lambda_{kk}) \cdot \mathbf{Re}_k = 0, \quad (18)$$

for each of the 7 waves k associated with block A_{AA} of (15). This condition is guaranteed by the fact that the complete solution for the inactive variables is taken to be the average of the input left and right states [8], and therefore the eigenvalues are constant with respect to each component of \mathbf{W}_A .

By analysis of the generalized Riemann invariants,

$$\frac{\partial(\mathbf{W}_A)_0}{\mathbf{e}_0^T \mathbf{Re}_k} = \frac{\partial(\mathbf{W}_A)_1}{\mathbf{e}_1^T \mathbf{Re}_k} = \dots = \frac{\partial(\mathbf{W}_A)_6}{\mathbf{e}_6^T \mathbf{Re}_k}, \quad (19)$$

for each wave k , it may be concluded (assuming for convenience $d = 0$) that

1. u_1 and τ_{10} are constant across the 5 contact (speed u_0) waves.
2. g_{01} and g_{11} are constant across the fast $u_0 \pm c_0$ waves.
3. The generalized Riemann invariants for the \pm fast waves include the identities

$$\frac{\partial u_1}{\pm c_0} = \frac{\partial \tau_{10}}{-\rho c_0^2} = \frac{\partial g_{00}}{g_{01}} = \frac{\partial g_{10}}{g_{11}}, \quad (20)$$

where the denominators of each term are constant across the wave. Thus, across each fast wave the change in u_1 is proportional to c_0 , etc.

4. Across the fast waves, the generalized Riemann invariants contain also

$$\frac{\partial \tau_{11}}{-2\tau_{10}}. \quad (21)$$

So, given the change of τ_{10} across the given wave, the change in τ_{11} is determined.

Let the constant states in the Riemann fan be labeled \mathbf{W}_L , \mathbf{W}_{L^*} , \mathbf{W}_{R^*} , and \mathbf{W}_R in sequence, and let Ψ_L (Ψ_R) measure the strength of the left (right) fast waves. From observation 3 one has:

$$\begin{aligned} \begin{pmatrix} u_1 \\ \tau_{10} \end{pmatrix}_{L^*} &= \begin{pmatrix} u_1 \\ \tau_{10} \end{pmatrix}_L - \Psi_L \begin{pmatrix} c_0 \\ \rho c_0^2 \end{pmatrix}, \\ \begin{pmatrix} u_1 \\ \tau_{10} \end{pmatrix}_{R^*} &= \begin{pmatrix} u_1 \\ \tau_{10} \end{pmatrix}_R + \Psi_R \begin{pmatrix} c_0 \\ -\rho c_0^2 \end{pmatrix}, \end{aligned} \quad (22)$$

and from observation 1 one has $(u_1, \tau_{10})_{L^*} = (u_1, \tau_{10})_{R^*}$, which couples the fast waves enabling their strength to be simply determined from:

$$\begin{pmatrix} c_0 & c_0 \\ \rho c_0^2 & -\rho c_0^2 \end{pmatrix} \begin{pmatrix} \Psi_L \\ \Psi_R \end{pmatrix} = \begin{pmatrix} u_1 \\ \tau_{10} \end{pmatrix}_L - \begin{pmatrix} u_1 \\ \tau_{10} \end{pmatrix}_R. \quad (23)$$

With τ_{10} determined across the wave fan, observation 4 determines τ_{11} :

$$\int_{(\tau_{11})_L}^{(\tau_{11})_{L^*}} d\tau_{11} = \frac{2}{\rho c_0^2} \int_{(\tau_{10})_L}^{(\tau_{10})_{L^*}} \tau_{10} d\tau_{10}, \quad (24)$$

$$(\tau_{11})_{L^*} = (\tau_{11})_L + \frac{1}{\rho c_0^2} [(\tau_{10})_{L^*}^2 - (\tau_{10})_L^2]. \quad (25)$$

The same equation holds across the right fast wave. The determination of other variables is then trivial by application of observation 3. For example, from (20):

$$\frac{(g_{10})_{R^*} - (g_{10})_R}{(g_{01})_{R^*}} = \frac{(u_1)_{R^*} - (u_1)_R}{c_0}. \quad (26)$$

The active variable solution to our Riemann problem is given by the constant state $(L, L^*, R^*, \text{ or } R)$ containing the zero wave speed characteristic.

3 Predictor-Corrector Formulation

We discretize time in steps Δt , with $t^{n+1} = t^n + \Delta t^n$. Space is discretized in square cells of length h , and $\mathbf{x} = h\mathbf{i}$ is the lower left corner of cell \mathbf{i} . Variables $\mathbf{U}_{\mathbf{i}}^n$ are cell-centered.

For each time step n , the artificial wave speed a is a global constant determined by the heuristic model:

$$a^2 = \min \left\{ \chi(\lambda) a_\infty^2 + [1 - \chi(\lambda)] a_0^2, \frac{\nu_p}{\lambda} \right\}, \quad (27)$$

$$a_\infty^2 = \frac{\nu_p}{\lambda}, \quad (28)$$

$$a_0^2 = \frac{2}{\rho} \min_{\mathbf{i}, d} |(\tau_{dd})_{\mathbf{i}}|, \quad (29)$$

$$\chi(\lambda) = \frac{\lambda}{t_{\text{adv}}} \left[1 - e^{-\lambda/(2t_{\text{adv}})} \right] \left(1 - e^{-t_{\text{adv}}/\lambda} \right), \quad (30)$$

$$t_{\text{adv}} = \frac{h}{\max_{\mathbf{i}} |\mathbf{u}|}, \quad (31)$$

with limiting values $a^2 = a_\infty^2$ as $\lambda \rightarrow \infty$, and $a^2 = a_0^2$ as $\lambda \rightarrow 0$. Note that the conserved quantity \mathbf{M} depends on a , so a reevaluation of a necessitates a rescaling of \mathbf{M} throughout the domain.

The predictor step of the method uses well-established higher-order Godunov approaches [5, 6] to estimate time-centered edge-centered solution values. These predictor states are made discrete divergence free ($\nabla \cdot \mathbf{u}^{n+\frac{1}{2}} = 0$) on a marker-and-cell (MAC) stencil [15].

Fluxes $\mathbf{F}_{\mathbf{i} \pm \mathbf{e}/2}^{n+\frac{1}{2}} = \mathbf{F}(\mathbf{U}_{\mathbf{i} \pm \mathbf{e}/2}^{n+\frac{1}{2}})$ computed from these predictor states enter a conservative update:

$$\tilde{\mathbf{U}}_{\mathbf{i}}^{n+1} = \mathbf{U}_{\mathbf{i}}^n - \frac{\Delta t}{h} \sum_{d=0}^{D-1} \left[(\mathbf{F}_d)_{\mathbf{i}+\mathbf{e}_d/2}^{n+\frac{1}{2}} - (\mathbf{F}_d)_{\mathbf{i}-\mathbf{e}_d/2}^{n+\frac{1}{2}} \right]. \quad (32)$$

The corrector computes \mathbf{U}^{n+1} by adding to $\tilde{\mathbf{U}}^{n+1}$ implicit and explicit source term contributions, and by use of an approximate cell-centered projection to make \mathbf{u}^{n+1} discrete divergence free.

3.1 Predictor

The predictor in our predictor-corrector method consists of the calculation of time-centered edge-centered states, $\mathbf{W}_{\mathbf{i}+\mathbf{e}_d/2}^{n+1/2}$, which are discrete divergence-free. The predictor state is computed in four steps.

First, the one-dimensional primitive equations are used to estimate time-centered edge-centered states. For the active partition, characteristic tracing and slope limiting occur as in higher-order Godunov methods. For the inactive partition, extrapolation in time with centered Taylor series are used. This first step uses strictly one-dimensional equations with no transverse coupling.

Second, the edge states so obtained are double-valued, and we resolve these with the Riemann solver described above in §2.0.1.

Third, the transverse coupling omitted in the first step is incorporated using cell-centered gradients of the edge-centered states computed by the Riemann solution. The transverse flux correction is described in [5, 28], but we include the transverse terms in terms of primitive variable differences rather than conservative fluxes. The corrected states so-obtained are again double-valued, and another Riemann problem gives a single final result.

Fourth, time-centered edge-centered velocity data is made discrete divergence-free, i.e.,

$$\mathbf{u} := \mathbf{u} - \nabla \left[\Delta^{-1} (\nabla \cdot \mathbf{u}) \right]. \quad (33)$$

With \mathbf{u} edge-centered, $\nabla \cdot \mathbf{u}$ is cell-centered. This projection is exact, in the sense that $\Delta_h = (\nabla \cdot)_h \nabla_h$, with the discrete Laplacian reducing to the standard 5-point stencil in 2D away from boundaries. Then, $\Delta^{-1} (\nabla \cdot \mathbf{u})$ is also cell-centered. The discrete gradient operator uses centered divided differences to give edge-centered corrections. The normal and tangential velocity components are updated at each face even though only the normal velocity contributes to the divergence.

The details of the first step is now given. With the “active”–“inactive” partitioning introduced in (13), upwind characteristic tracing for the active primitive variables takes the form:

$$(\tilde{\mathbf{W}}_{A,d})_{\mathbf{i}+\mathbf{e}_d/2,L}^{n+\frac{1}{2}} = (\mathbf{W}_{A,d})_{\mathbf{i}}^n - \mathbf{R}_d \mathcal{P}_+ \left(\frac{\Delta t}{2} \Lambda_d - \frac{h}{2} \mathbf{I} \right) \mathbf{R}_d^{-1} \left(\frac{\partial \mathbf{W}_{A,d}}{\partial x_d} \right)_{\mathbf{i}}^n$$

$$\begin{aligned}
& -\frac{\Delta t}{2h} \mathbf{A}_{AI,d} \left(\frac{\partial \mathbf{W}_{I,d}}{\partial x_d} \right)_{\mathbf{i}}^n, \tag{34} \\
(\tilde{\mathbf{W}}_{A,d})_{\mathbf{i}+\mathbf{e}_d/2,R}^{n+\frac{1}{2}} &= (\mathbf{W}_{A,d})_{\mathbf{i}+\mathbf{e}_d}^n - \mathbf{R}_d \mathcal{P}_- \left(\frac{\Delta t}{2} \mathbf{\Lambda}_d + \frac{h}{2} \mathbf{I} \right) \mathbf{R}_d^{-1} \left(\frac{\partial \mathbf{W}_{A,d}}{\partial x_d} \right)_{\mathbf{i}+\mathbf{e}_d}^n \\
& -\frac{\Delta t}{2h} \mathbf{A}_{AI,d} \left(\frac{\partial \mathbf{W}_{I,d}}{\partial x_d} \right)_{\mathbf{i}+\mathbf{e}_d}^n, \tag{35}
\end{aligned}$$

where $\mathcal{P}_{\pm}(\mathcal{D}) = \text{diag}(\mathcal{D}_{ii} \text{ if } \Lambda_{ii} \gtrless 0, 0 \text{ otherwise})$ is a projection that sets to zero those terms of the diagonal argument matrix corresponding with eigenvalues whose sign is negative/positive, respectively. The subscript L (R) indicates that the result is traced to the left (right) side of the edge $\mathbf{i}+\mathbf{e}_d/2$. Where the stencils support it, the derivatives $\partial \mathbf{W}_A/\partial x$ use van-Leer limited [34] fourth-order accurate derivatives [4]. The derivatives $\partial \mathbf{W}_I/\partial x$ use second-order centered divided differences. The tilde denotes that source terms have not yet been accounted for. The inactive variables are extrapolated in time using

$$\begin{aligned}
(\tilde{\mathbf{W}}_{I,d})_{\mathbf{i}+\mathbf{e}_d/2,L}^{n+\frac{1}{2}} &= (\tilde{\mathbf{W}}_{I,d})_{\mathbf{i}}^n - \left(\frac{\Delta t}{2} \mathbf{A}_{II,d} - \frac{h}{2} \mathbf{I} \right) \left(\frac{\partial \mathbf{W}_{I,d}}{\partial x_d} \right)_{\mathbf{i}}^n \\
& -\frac{\Delta t}{2} \mathbf{A}_{IA,d} \left(\frac{\partial \mathbf{W}_{A,d}}{\partial x_d} \right)_{\mathbf{i}}^n, \tag{36}
\end{aligned}$$

$$\begin{aligned}
(\tilde{\mathbf{W}}_{I,d})_{\mathbf{i}+\mathbf{e}_d/2,R}^{n+\frac{1}{2}} &= (\tilde{\mathbf{W}}_{I,d})_{\mathbf{i}+1}^n - \left(\frac{\Delta t}{2} \mathbf{A}_{II,d} + \frac{h}{2} \mathbf{I} \right) \left(\frac{\partial \mathbf{W}_{I,d}}{\partial x_d} \right)_{\mathbf{i}+\mathbf{e}_d}^n \\
& -\frac{\Delta t}{2} \mathbf{A}_{IA,d} \left(\frac{\partial \mathbf{W}_{A,d}}{\partial x_d} \right)_{\mathbf{i}+\mathbf{e}_d}^n. \tag{37}
\end{aligned}$$

The velocity source is computed explicitly via:

$$\mathbf{u}_{\mathbf{i}+\mathbf{e}_d/2,L}^{n+\frac{1}{2}} = \tilde{\mathbf{u}}_{\mathbf{i}+\mathbf{e}_d/2,L}^{n+\frac{1}{2}} + \frac{\Delta t}{2} \left[-\frac{1}{\rho} \nabla p_{\mathbf{i}}^{n-\frac{1}{2}} + \nu_s (\Delta_h \mathbf{u}^n)_{\mathbf{i}} \right], \tag{38}$$

where Δ_h the discrete 5-point Laplacian in regular domains. The time-centered pressure is taken from the previous time step. The calculation of $\nabla p^{n+\frac{1}{2}}$ occurs as the last step of the corrector, (45).

The source term for viscoelastic stress is computed implicitly to properly recover the Newtonian limit ($\boldsymbol{\tau} \rightarrow 2\mu_p \mathbf{D}$ as $\lambda \rightarrow 0$):

$$\boldsymbol{\tau}_{\mathbf{i}+\mathbf{e}_d/2,L}^{n+\frac{1}{2}} = \tilde{\boldsymbol{\tau}}_{\mathbf{i}+\mathbf{e}_d/2,L}^{n+\frac{1}{2}} + \frac{\Delta t}{2} \left[-\frac{1}{\lambda} \boldsymbol{\tau}_{\mathbf{i}+\mathbf{e}_d/2,L}^{n+\frac{1}{2}} + \left(\frac{\mu_p}{\lambda} - \rho a^2 \right) 2\mathbf{D}_{\mathbf{i}}^n \right]. \tag{39}$$

The rate of strain tensor, \mathbf{D} , is calculated with centered differences.

The source terms for \mathbf{g} are omitted for the following reason. The material reference frame \mathbf{X} can be defined, at the start of each time step, to be equal to \mathbf{x} , i.e., $\mathbf{g} = \mathbf{I}$ identically at the start of each time step. With this choice, the source terms for \mathbf{g} are zero if evaluated at t^n . Resetting \mathbf{g} to \mathbf{I} necessitates renormalizing \mathbf{M} from time step to time step.

3.2 Corrector

The corrector generates time $n+1$ cell-centered states that are discrete divergence free. The basic idea is to generate cell-centered time t^{n+1} estimates, $\tilde{\mathbf{U}}^{n+1}$, using the flux differencing quadrature (32). To these estimates source terms are added, as described below, to obtain \mathbf{U}^{n+1} .

The corrector step for the velocity field is more complicated. We would like to use the following update equation (the superscript $*$ indicates that the velocity field is not yet divergence free):

$$\frac{\mathbf{u}^{n+1,*} - \mathbf{u}^n}{\Delta t} = \left[-\nabla \cdot (\mathbf{u} \otimes \mathbf{u} - \frac{1}{\rho} \boldsymbol{\tau})^{n+\frac{1}{2}} \right] + \left(-\frac{1}{\rho} \nabla p^{n-\frac{1}{2}} + \nu_s \Delta \mathbf{u} \right). \quad (40)$$

However, as in [30], we would like for the velocity update equation to properly capture the Newtonian and elastic limits. We modify the predictor step by not including the source terms for $\boldsymbol{\tau}$ in the edge state prediction to instead obtain $\tilde{\boldsymbol{\tau}}$ at edges. However, extra care must be taken since the transverse correction term is still computed with edge states that have been constructed with the $\boldsymbol{\tau}$ sources.

Combining an equation of the form (39) with (40), we arrive at our new update equation for velocity:

$$\begin{aligned} \frac{\mathbf{u}^{n+1,*} - \mathbf{u}^n}{\Delta t} = & \left[\nu_s + \frac{\Delta t(\nu_p - \lambda a^2)}{2\lambda + \Delta t} \right] \Delta \mathbf{u} + \\ & \left[-\nabla \cdot \left(\mathbf{u} \otimes \mathbf{u} - \frac{2\lambda}{2\lambda + \Delta t} \frac{\tilde{\boldsymbol{\tau}}}{\rho} \right)^{n+\frac{1}{2}} - \frac{1}{\rho} \nabla p^{n-\frac{1}{2}} \right]. \end{aligned} \quad (41)$$

These equations are expressible as D scalar discrete Helmholtz equations. This discretization is chosen in order to capture the Newtonian and elastic limits, i.e., in the Newtonian limit ($\lambda \rightarrow 0$) we recover:

$$\frac{\mathbf{u}^{n+1,*} - \mathbf{u}^n}{\Delta t} = [\nu_s + \nu_p] \Delta \mathbf{u} + \left[-\nabla \cdot (\mathbf{u} \otimes \mathbf{u})^{n+\frac{1}{2}} - \frac{1}{\rho} \nabla p^{n-\frac{1}{2}} \right], \quad (42)$$

and in the elastic limit ($\lambda \rightarrow \infty$), where a^2 is given by (28), we recover:

$$\frac{\mathbf{u}^{n+1,*} - \mathbf{u}^n}{\Delta t} = \nu_s \Delta \mathbf{u} + \left[-\nabla \cdot \left(\mathbf{u} \otimes \mathbf{u} - \frac{\tilde{\boldsymbol{\tau}}}{\rho} \right)^{n+\frac{1}{2}} - \frac{1}{\rho} \nabla p^{n-\frac{1}{2}} \right]. \quad (43)$$

The Helmholtz equations (41) are solved using the Runge-Kutta technique of [32], which yields an l_0 stable solution in regular and irregular domains. That method specifies the time centering of the Laplacian term.

The last step of the velocity corrector removes the divergence of \mathbf{u}^* and calculates the pressure whose gradient will affect the subsequent time step using a pressure-projection formulation [31]. First, a potential ϕ is calculated on cell centers with the discrete Laplacian:

$$\Delta \phi = \left[\nabla \cdot \underset{\text{CC} \rightarrow \text{FC}}{\text{Avg}} \left(\mathbf{u}^{n+1,*} + \frac{\Delta t}{\rho} \nabla p^{n-\frac{1}{2}} \right) \right]. \quad (44)$$

Pressure is proportional to ϕ , and :

$$\nabla p^{n+\frac{1}{2}} = \frac{\rho}{\Delta t} \nabla \phi. \quad (45)$$

With this gradient, the discrete-divergence-free velocity is

$$\mathbf{u}^{n+1} = \mathbf{u}^{n+1,*} + \frac{\Delta t}{\rho} \left(\nabla p^{n-\frac{1}{2}} - \nabla p^{n+\frac{1}{2}} \right). \quad (46)$$

This projection is approximate, in the sense that $\Delta_h \neq (\nabla \cdot)_h \nabla_h$. As noted by [20], the approximate projection does not remove certain non-physical oscillatory modes. These are damped by application of a filter

$$\mathbf{u} := \mathbf{u} + \zeta \nabla (\nabla \cdot \mathbf{u}), \quad (47)$$

using a divergence stencil other than the centered divided difference used in (44). We use $\zeta = h^2/5$ in 2D which is stable while always damping monopole modes in the experience of [8, 30].

The corrector step for \mathbf{g} and \mathbf{M} simply follows the flux differencing quadrature (32) followed by a source term update. The source term for \mathbf{g} is computed as in [23] using edge- and time-centered values from the predictor. The viscoelastic stress source term is discretized using Crank-Nicholson:

$$\begin{aligned} \mathbf{M}^{n+1} = \tilde{\mathbf{M}}^{n+1} &+ \frac{\Delta t}{2} \left(\mathbf{g} \left[\left(\frac{\mu_p}{\lambda} - \rho a^2 \right) 2\mathbf{D} - \frac{1}{\lambda} \boldsymbol{\tau} \right] \mathbf{g}^T \right)^n \\ &+ \frac{\Delta t}{2} \left(\mathbf{g} \left[\left(\frac{\mu_p}{\lambda} - \rho a^2 \right) 2\mathbf{D} - \frac{1}{\lambda} \boldsymbol{\tau} \right] \mathbf{g}^T \right)^{n+1}, \end{aligned} \quad (48)$$

rearranged in the form:

$$\begin{aligned} \mathbf{M}^{n+1} &= \frac{2\lambda}{2\lambda + \Delta t} \tilde{\mathbf{M}}^{n+1} - \frac{\Delta t}{2\lambda + \Delta t} \mathbf{M}^n \\ &+ \frac{\Delta t}{2\lambda + \Delta t} \left(\mathbf{g} [(\mu_p - \rho a^2 \lambda) 2\mathbf{D} + \rho a^2 \mathbf{I}] \mathbf{g}^T \right)^n \\ &+ \frac{\Delta t}{2\lambda + \Delta t} \left(\mathbf{g} [(\mu_p - \rho a^2 \lambda) 2\mathbf{D} + \rho a^2 \mathbf{I}] \mathbf{g}^T \right)^{n+1}, \end{aligned} \quad (49)$$

which is evaluated point-wise.

4 Irregular Domains

We use a Cartesian grid embedded boundary method to discretize the fluid equations in the presence of irregular boundaries. In this approach, the irregular domain is discretized as a collection of control volumes formed by the intersection of the problem domain with the square Cartesian grid cells as in a “cookie-cutter”. The various operators – the discrete divergence $\nabla \cdot$, discrete gradient ∇ , and discrete Laplacian Δ – are approximated using finite volume differences on the irregular

control volumes. Cells are classified as regular if they do not intersect embedded boundaries, irregular if they intersect boundaries, or covered if they have zero fluid volume fraction. Faces are classified in an analogous way. In problems containing irregular domains, the finite volume treatment of the regular cells follows the description of §3.

Throughout, time t^n data (\mathbf{U}) will be centered at cell centers, even if that point lies outside the fluid domain. Time $t^{n+\frac{1}{2}}$ data (fluxes \mathbf{F}) are centered at the centroid of faces,

$$\hat{\mathbf{x}}_{\mathbf{i}\pm\mathbf{e}_d/2} = \frac{1}{\alpha_{\mathbf{i}\pm\mathbf{e}_d/2} h^{D-1}} \int_{A_{\mathbf{i}\pm\mathbf{e}_d/2}} \mathbf{x} dA, \quad (50)$$

where $\alpha_{\mathbf{i}\pm\mathbf{e}_d/2}$ is the area fraction of a cell edge $\mathbf{i}\pm\mathbf{e}_d/2$ not covered by the embedded boundary, or:

$$\alpha_{\mathbf{i}+\mathbf{e}_d/2} = \frac{A_{\mathbf{i}+\mathbf{e}_d/2}}{h^{D-1}}, \quad (51)$$

with $A_{\mathbf{i}\pm\mathbf{e}_d}$ the area of cell \mathbf{i} on side $\pm d$ in contact with the fluid. Other geometric quantities used are the volume fraction, defined as:

$$\kappa_{\mathbf{i}} = \frac{V_{\mathbf{i}}}{h^D}, \quad (52)$$

the area fraction of the domain boundary intersected with cell \mathbf{i} , $A_{\mathbf{i}}^{\text{EB}}$, and its associated area fraction, defined as:

$$\alpha_{\mathbf{i}}^{\text{EB}} = \frac{A_{\mathbf{i}}^{\text{EB}}}{h^{D-1}}, \quad (53)$$

and the outward-directed vector normal to the embedded boundary interface in cell \mathbf{i} , given by:

$$\mathbf{n}_{\mathbf{i}} = \frac{1}{\alpha_{\mathbf{i}\pm\mathbf{e}_d/2} h^{D-1}} \int_{A_{\mathbf{i}}^{\text{EB}}} \mathbf{n} dA. \quad (54)$$

In irregular cells, the quadrature (32) is not appropriate [6]. A stable but non-conservative update is:

$$\tilde{\mathbf{U}}_{\mathbf{i}}^{n+1} = \mathbf{U}_{\mathbf{i}}^n - \Delta t \left[\kappa_{\mathbf{i}} (\nabla \cdot \mathbf{F})_{\mathbf{i}}^{\text{C}} + (1 - \kappa_{\mathbf{i}}) (\nabla \cdot \mathbf{F})_{\mathbf{i}}^{\text{NC}} \right]^{n+\frac{1}{2}}, \quad (55)$$

with conservative and non-conservative flux differences given by:

$$(\nabla \cdot \mathbf{F})_{\mathbf{i}}^{\text{NC}} = \frac{1}{h} \sum_{d=0}^{D-1} [(\mathbf{F}_d)_{\mathbf{i}+\mathbf{e}_d/2} - (\mathbf{F}_d)_{\mathbf{i}-\mathbf{e}_d/2}], \quad (56)$$

$$\begin{aligned} (\nabla \cdot \mathbf{F})_{\mathbf{i}}^{\text{C}} &= \frac{1}{V_{\mathbf{i}}} \int_{V_{\mathbf{i}}} (\nabla \cdot \mathbf{F}) dV \\ &\approx \frac{1}{\kappa_{\mathbf{i}} h} \left[\sum_{d=0}^{D-1} \sum_{\pm} [\pm \alpha_{\mathbf{i}\pm\mathbf{e}_d/2} (\mathbf{F}_d)_{\mathbf{i}\pm\mathbf{e}_d/2}] + \alpha_{\mathbf{i}}^{\text{EB}} (\mathbf{n}_{\mathbf{i}} \cdot \mathbf{F}_{\mathbf{i}}^{\text{EB}}) \right], \end{aligned} \quad (57)$$

respectively.

Conservation violation is expressed locally by the generalized mass deficit $\delta \mathbf{m}$,

$$\delta \mathbf{m}_{\mathbf{i}} = \Delta t (1 - \kappa_{\mathbf{i}}) \kappa_{\mathbf{i}} [(\nabla \cdot \mathbf{F})^{\text{NC}} - (\nabla \cdot \mathbf{F})^{\text{C}}]_{\mathbf{i}}, \quad (58)$$

which is redistributed according to:

$$\tilde{\mathbf{U}}_{\mathbf{i}}^{n+1} := \tilde{\mathbf{U}}_{\mathbf{i}}^{n+1} + \sum_{\mathbf{j}=\text{neighbor}(\mathbf{i})}^{3^D} \frac{\delta \mathbf{m}_{\mathbf{j}}}{w_{\mathbf{j}}}, \quad (59)$$

$$w_{\mathbf{i}} = \sum_{\mathbf{j}=\text{neighbor}(\mathbf{i})}^{3^D} \kappa_{\mathbf{j}}. \quad (60)$$

The calculation of fluxes on covered faces, and stencils used to re-center fluxes to centroids, are described in [6, 22, 29]. Additional details are given in [24]. Here we describe differences between the regular and irregular domain calculations that are specific to the present algorithm.

We compute the Poisson equation in divergence form, $\Delta \phi \approx \nabla^h \cdot (\nabla^h \phi) = f$, with discrete divergence given by the conservative form (57). This means that $\kappa \Delta^h \phi$ is directly accessible, and division by κ can be unstable. For the Laplacian appearing in the velocity source term (38) we use $\kappa \Delta^h \phi$ in place of $\Delta^h \phi$, which formally introduces an $\mathcal{O}(\Delta t)$ discretization error. However, the results obtained by this approximation are stable and appear to not affect the global error.

In irregular cells the discretization of the divergence term in (41) is computed as follows. Define a velocity flux to be:

$$\mathbf{F}_{\mathbf{u}} = \mathbf{u} \otimes \mathbf{u} - \frac{2\lambda}{2\lambda + \Delta t} \frac{\tilde{\boldsymbol{\tau}}}{\rho}. \quad (61)$$

Then, compute the divergence of $\mathbf{F}_{\mathbf{u}}$ using (55) and redistribute according to (59).

Covered face values needed in the non-conservative divergence are obtained by extrapolation from face-centered time-centered values, as described in [6]. Unlike [6], we take this extrapolated edge state to represent the unique face value, so no further Riemann problem is solved.

5 Boundary Conditions

In the hyperbolic treatment, boundary conditions enter in two ways:

1. on embedded boundaries, e.g., the computation of \mathbf{F}^{EB} in (57); and
2. where the Cartesian cells abut the problem domain.

The conservative flux divergence (57) includes the flux derived from data centered at the centroid of the embedded boundary. Such states are derived from

cell-centered data using Taylor series, without upwind projection. If $\hat{\mathbf{x}}_i^{\text{EB}}$ is the centroid relative to the cell center,

$$\begin{aligned}\mathbf{W}_i^{n+\frac{1}{2},\text{EB}} &= \mathbf{W}_i^n + \hat{\mathbf{x}}_i^{\text{EB}} \cdot (\nabla \mathbf{W}^n)_i + \frac{\Delta t}{2} \left(\frac{\partial \mathbf{W}_i}{\partial t} \right)^n \\ &= \mathbf{W}_i^n + \sum_d \left[(\hat{\mathbf{x}}_i^{\text{EB}})_d \mathbf{I} - \frac{\Delta t}{2} \mathbf{A}_d \right] \left(\frac{\partial \mathbf{W}^n}{\partial x_d} \right)_i + \frac{\Delta t}{2} \mathbf{S}_i^n.\end{aligned}\quad (62)$$

This extrapolation is implemented without partitioning of \mathbf{W} or \mathbf{A} . The source terms are implemented as with the predictor §3.1. The discrete gradient $\nabla \mathbf{W}$ uses central differences where possible, or one-sided differences where necessary.

This one-sided boundary value may be incompatible with physical boundary conditions. The approach to boundary conditions uses the ideas of [10]. Let \mathbf{W}_P be an extrapolated edge state, as calculated by (62), and let \mathbf{W}_S be the final value used to construct the edge flux. In appropriately rotated coordinates, we are interested in the eigenstructure of the matrix $\mathbf{A}_{AA}(\mathbf{W}_S)$. For each characteristic pointing into the domain, one degree of freedom at the boundary must be specified. For each characteristic pointing out of the domain, a characteristic condition must be met. Specifically, if characteristic k points out of the domain, a sufficient characteristic condition is

$$\mathbf{l}_k \cdot (\mathbf{W}_P - \mathbf{W}_S) = 0. \quad (63)$$

For solid wall boundaries, including the embedded boundaries, this construction is straightforward. We derive \mathbf{A}_{AA} on the boundary using active variables taken from \mathbf{W}_P , and selecting inactive variables on physical grounds. In the present application, the embedded boundaries are stationary surfaces subject to no-flow conditions. Accordingly, the inactive variable u_n is uniquely determined, $u_n = 0$ (here subscript n denotes the interface normal direction; subscript t will denote the tangential direction). There is no *a priori* reason for τ_{nn} to be affected by boundary conditions, thus we take τ_{nn} in state \mathbf{W}_S equal to its extrapolated value in \mathbf{W}_P . With these choices, exactly one characteristic of \mathbf{A}_{AA} enters the domain, leaving one degree of freedom to be specified. We use the no-slip boundary condition to zero the tangential velocity component. For the characteristic that points out of the domain, the characteristic condition $\mathbf{l}_{u_n-c} \cdot (\mathbf{W}_P - \mathbf{W}_S) = 0$ (if the wall normal is positive) or $\mathbf{l}_{u_n+c} \cdot (\mathbf{W}_P - \mathbf{W}_S) = 0$ (if the wall normal is negative) uniquely determines the shear stress τ_{nt} component of \mathbf{W}_S . Thus, for solid wall boundaries, $\mathbf{W}_S = \mathbf{W}_P$, except for variables \mathbf{u} which are taken to be zero on physical grounds and the shear stress which is determined by the characteristic condition.

For inflow and outflow boundaries this procedure is more involved. Let \mathbf{n} point out of the domain, so for inflow we have $u_n < 0$. Inflow conditions are either supersonic, $u_n + c < 0$, or not, with u_n and c given by inactive variables taken from the specified inflow condition. When supersonic, all characteristics flow into the domain, and the state \mathbf{W}_S is given exclusively by imposed conditions. If not supersonic, only the characteristic $u_n + c$ flows out of the domain, so only one constraint on \mathbf{W}_S comes from \mathbf{W}_P . In this case we determine the shear stress τ_{nt}

component of \mathbf{W}_S by solving $\mathbf{l}_{u_n+c} \cdot (\mathbf{W}_P - \mathbf{W}_S) = 0$, with all other components of \mathbf{W}_S being prescribed by the inflow condition.

On outflow, we take the inactive variables from \mathbf{W}_P , and $u_n > 0$. If supersonic, $u_n - c > 0$, no characteristics flow into the fluid domain, and we take $\mathbf{W}_S = \mathbf{W}_P$. If subsonic, one degree of freedom of \mathbf{W}_S is specified by external conditions. In that case, we choose $u_t = 0$ and determine the remaining values of \mathbf{W}_S from $\mathbf{l}_k \cdot (\mathbf{W}_S - \mathbf{W}_P) = 0, \forall k \neq u_n - c$.

Boundary conditions are also required for the Helmholtz velocity correctors, (41), and the divergence-cleaning projections (33) and (44). The implicit velocity equations (41) use homogeneous Dirichlet conditions on solid wall boundaries, inhomogeneous Dirichlet conditions on inflow boundaries (using prescribed far-field values), and homogeneous Neumann conditions on outflow. The discrete Laplacian operator encountered in divergence-cleaning projections uses homogeneous Dirichlet on outflow, and homogeneous Neumann on inflow and solid walls.

6 Results

Results are presented for three fluids: a Maxwell (highly elastic) fluid, characterized by having no solvent viscosity, a non-zero polymeric viscosity, and a non-zero relaxation time; a Newtonian fluid, characterized by having a non-zero solvent viscosity, no polymeric viscosity, and relaxation time of zero; and a hybrid fluid [30] – a Maxwell fluid with an added solvent viscosity. Two geometries are used that are nonconforming with Cartesian grids; a rotated rectangular geometry, and a circular domain.

For the rectangular geometry, the computational domain has $l = w = 2.0$. The rectangular box has dimensions $l = 1.7$, and $w = 1.0$, and has been rotated 45° to maximize the amount of fluid in the computational domain. The coarse domain has 128×128 cells. We have chosen an initial vortex velocity profile that is sufficiently smooth at the vortex edge, given by the function $u_\theta(r) = 2.56[(r/0.45)(1 - r/0.45)]^4 H(0.45 - r)$, where r is the distance to the center of the box and H is the Heaviside step function. This gives a maximum initial speed of $|\mathbf{u}| = 1.0$ at $r = 0.225$ (see Figure 1, top-left).

For all images corresponding to the angled box geometry, we have rotated the output so the variables are seen with respect to the normal (length-wise) and transverse (width-wise) directions. The initial pressure is set to zero. We define the characteristic speed, U , as the maximum initial velocity and the characteristic length, L , as the width of the box.

For the circular geometry, the computational domain has $l = w = 1.0$ and the circle has radius $r = 0.45$ to maximize the amount of fluid in the computational domain. The coarse domain has 64×64 cells. The initial velocity profile is $u_\theta(r) = 2.56[(r/0.4)(1 - r/0.4)]^4 H(0.4 - r)$, which gives a maximum initial speed of $|\mathbf{u}| = 1.0$ at $r = 0.2$ (see Figure 3, top-left). The initial pressure is set to zero. We define the characteristic speed, U , as the maximum initial velocity and the characteristic length, L , as the diameter of the circle.

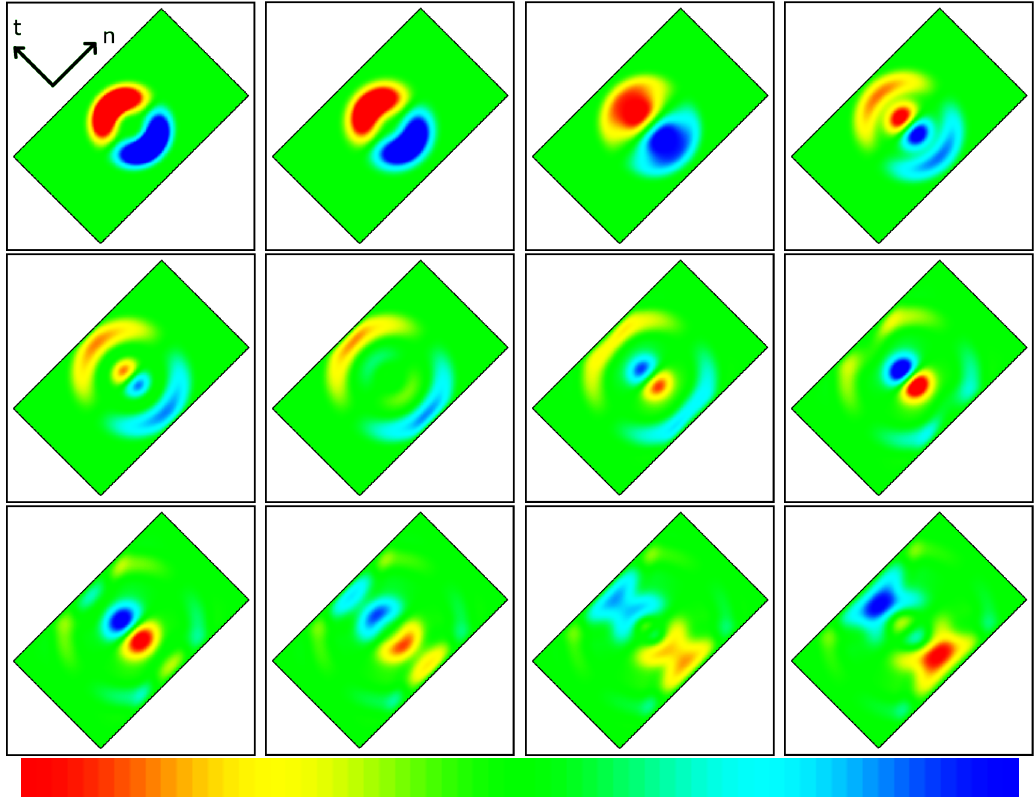


Figure 1: Time-dependent u_n profiles of a Maxwell fluid with a vortex initial condition in a rectangle. The domain has 256×256 cells with 24 time step increments using $\Delta t = 1.6 \times 10^{-3}$, -0.5 (red) to 0.5 (blue).

6.1 Maxwell Fluid

For the Maxwell fluid, the rheological parameters are $\mu_s = 0, \mu_p = 1.0, \lambda = 1.0$, and $\rho = 1.0$. This gives the dimensionless parameters $\text{Re} = 1.0, \text{We} = 1.0$, and $\text{Ma} = 1.0$ for the rectangular box geometry. The coarse time step for each geometry is 3.2×10^{-3} , corresponding to $\text{CFL} \approx 0.5$. The time-dependent normal velocity is shown in Figure 1. The elastic wave propagation and reflection off the walls is clearly visible. The transverse velocity, stress, and pressure corresponding to the final image of normal velocity are shown in Figure 2. The solution error convergence after 400 fine time steps is given in Table 1. We use the same rheological parameters for the circular geometry, leading to dimensionless parameters $\text{Re} = 0.9, \text{We} = 0.9$, and $\text{Ma} = 1.0$. The time-dependent u_0 profiles are shown in Figure 3. Again, the elastic wave propagation and reflection off the walls is easily visible. The u_1 component of velocity, stress, and pressure corresponding to the final image of u_0 are shown in Figure 4. The solution error convergence after 400 fine time steps is given in Table 2.

For Maxwell fluids, we have observed that additional cell-centered filtering steps

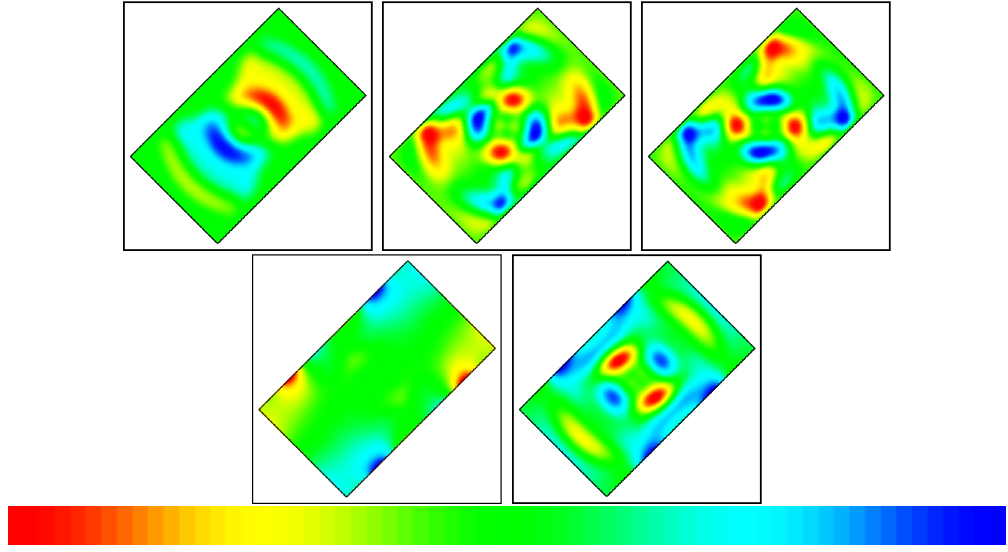


Figure 2: Profiles for a Maxwell fluid in a rectangle at $t = 0.4224$ (corresponding to the last image in Figure 1.) In order, clockwise from top-left: u_t , -0.5 (red) to 0.5 (blue); normal stress τ_{nn} , -0.21 (red) to 0.31 (blue); normal stress τ_{tt} , -0.21 (red) to 0.28 (blue); shear stress τ_{tn} , -0.46 (red) to 0.33 (blue); hydrostatic pressure p , 0 (red) to 0.656 (blue).

norm	Variable	Coarse Error	Fine Error	Order
L_1	u_0	9.90e-04	2.69e-04	1.88
	u_1	9.62e-04	2.63e-04	1.87
	τ_{00}	1.24e-03	3.06e-04	2.02
	τ_{10}	1.38e-03	3.40e-04	2.02
	τ_{11}	1.37e-03	3.39e-04	2.01
	p	1.04e-03	2.68e-04	1.96
L_2	u_0	1.65e-03	4.34e-04	1.93
	u_1	1.66e-03	4.23e-04	1.97
	τ_{00}	1.89e-03	4.78e-04	1.98
	τ_{10}	3.06e-03	6.93e-04	2.14
	τ_{11}	3.27e-03	8.36e-04	1.97
	p	2.52e-03	4.78e-04	2.40
L_∞	u_0	4.08e-02	6.32e-03	2.69
	u_1	4.15e-02	6.98e-03	2.57
	τ_{00}	5.11e-02	1.09e-02	2.23
	τ_{10}	8.36e-02	2.77e-02	1.59
	τ_{11}	1.45e-01	3.73e-02	1.95
	p	7.76e-02	1.15e-02	2.75

Table 1: Solution error convergence rates for a Maxwell fluid with a vortex initial condition in a rectangle. Data corresponds with Figs. 1 and 2.

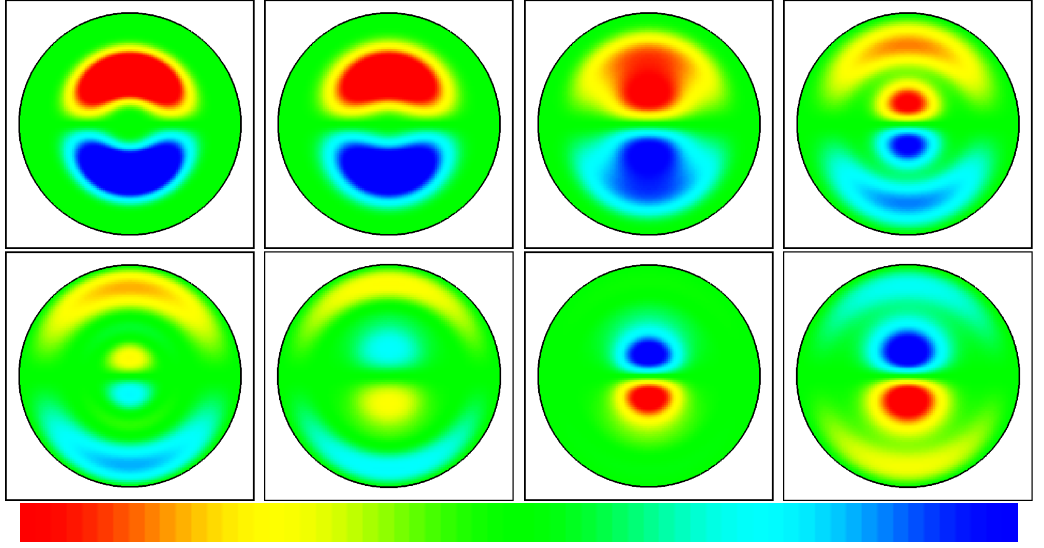


Figure 3: Time-dependent u_0 profiles of a Maxwell fluid with a vortex initial condition in a disk. The domain has 128×128 cells with 24 time step increments using $\Delta t = 1.6 \times 10^{-3}$, -0.50 (red) to 0.50 (blue).

(47) are required to prevent the buildup of divergent modes near cells with small volume fractions. In the other flow regimes, the non-zero solvent viscosity in the diffusion equation solver smooths the velocity and helps eliminate the divergent modes and additional filtering steps are not required. The approach taken here to stabilize the method is to perform 1 filter iteration per time step at the coarse resolution, 2 iterations at the medium resolution, and 4 iterations at the fine resolution. The additional filter steps are not required for the other flow regimes, but are included for consistency.

6.2 Newtonian Fluid

For the Newtonian fluid, the rheological parameters are $\mu_s = 1.0$, $\mu_p = 0.0$, $\lambda = 1.0 \times 10^{-11}$, and $\rho = 1.0$ leading to dimensionless parameters $\text{Re} = 1.0$ and $\text{We} = 0.0$ for the rectangular box geometry. Since $\mu_p = 0$, the polymeric stress remains zero at all times. The coarse time step for each geometry is 7.5×10^{-3} , corresponding to $\text{CFL} \approx 0.5$. The time-dependent normal velocity is shown in Figure 5, in which the vortex spreads out to fill the box and decays over time. The transverse velocity and pressure corresponding to the final image of normal velocity are shown in Figure 6. The solution error convergence after 40 fine time steps is given in Table 3. Only a small number of time steps are used because after 40 the fluid velocity has already decayed to less than two percent of its initial value. We use the same rheological parameters for the circular geometry, leading to dimensionless parameters $\text{Re} = 0.9$ and $\text{We} = 0$. The time-dependent normal velocity is shown in Figure 7. As with the rectangular box case, the vortex spreads out to fill the circle and decays over time.

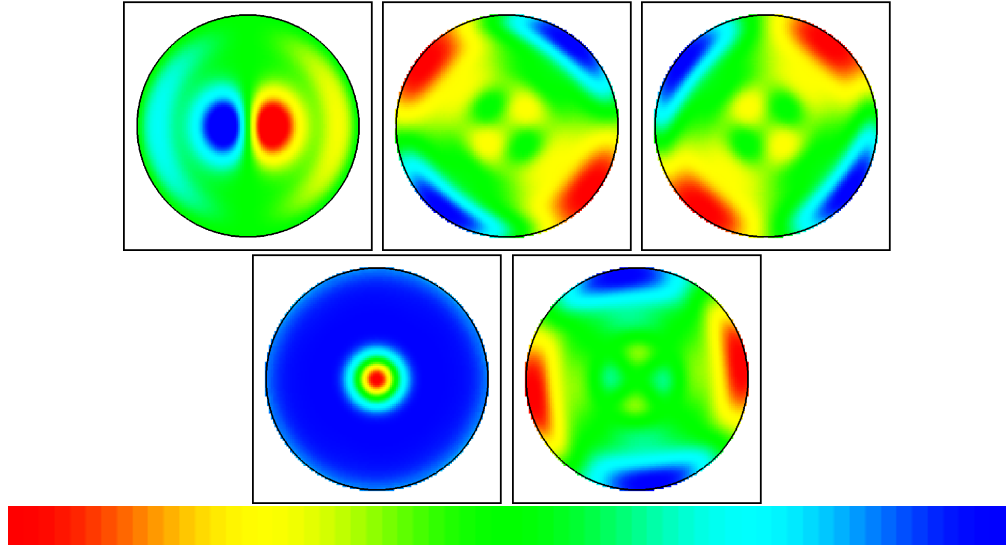


Figure 4: Profiles for a Maxwell fluid in a disk at $t = 0.2688$ (corresponding to the last image in Figure 3.) In order, clockwise from top-left: u_1 , -0.50 (red) to 0.50 (blue); normal stress τ_{00} , -0.38 (red) to 0.67 (blue); normal stress τ_{11} , -0.38 (red) to 0.67 (blue); shear stress τ_{10} , -0.53 (red) to 0.53 (blue); hydrostatic pressure p , 0 (red) to 0.55 (blue).

norm	Variable	Coarse Error	Fine Error	Order
L_1	u_0	2.00e-03	5.70e-04	1.81
	u_1	2.05e-03	6.14e-04	1.74
	τ_{00}	2.01e-03	6.87e-04	1.55
	τ_{10}	1.62e-03	6.87e-04	1.39
	τ_{11}	2.03e-03	6.88e-04	1.56
	p	1.49e-03	5.62e-04	1.40
L_2	u_0	3.06e-03	1.01e-03	1.59
	u_1	3.15e-03	1.08e-03	1.55
	τ_{00}	3.09e-03	1.02e-03	1.60
	τ_{10}	2.33e-03	8.78e-04	1.41
	τ_{11}	3.00e-03	1.00e-03	1.58
	p	2.19e-03	8.60e-04	1.35
L_∞	u_0	3.11e-02	1.66e-02	0.91
	u_1	3.31e-02	1.64e-02	1.01
	τ_{00}	4.07e-02	2.24e-02	0.86
	τ_{10}	4.15e-02	1.94e-02	1.09
	τ_{11}	3.68e-02	2.31e-02	0.67
	p	3.04e-02	2.16e-02	0.49

Table 2: Solution error convergence rates for a Maxwell fluid with a vortex initial condition in a disk. Data corresponds with Figs. 3 and 4.

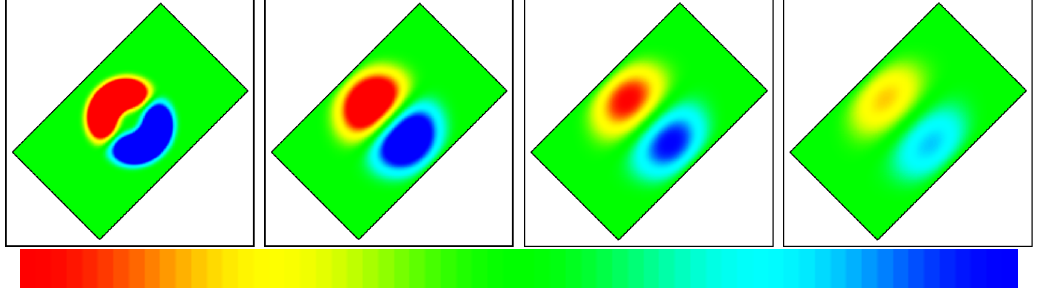


Figure 5: Time-dependent u_n profiles of a Newtonian fluid with a vortex initial condition in a rectangle. The domain has 256×256 cells with 2 time step increments using $\Delta t = 3.75 \times 10^{-3}$, -0.25 (red) to 0.25 (blue).

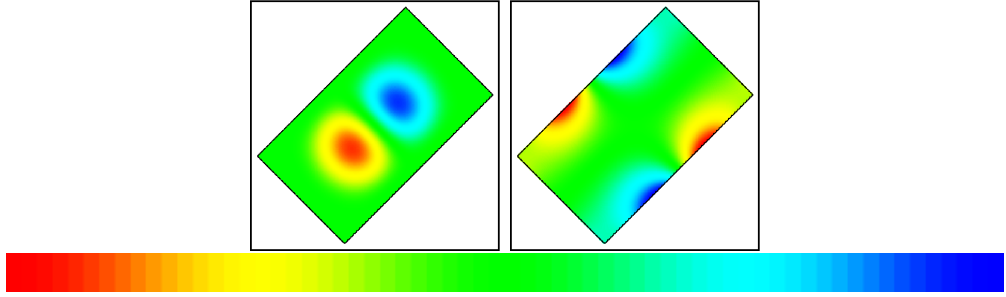


Figure 6: Profiles for a Newtonian fluid in a rectangle at $t = 2.25 \times 10^{-2}$ (corresponding to the last image in Figure 5.) (Left) u_t , -0.15 (red) to 0.15 (blue); (Right) hydrostatic pressure p , 0 (red) to 1.96 (blue).

norm	Variable	Coarse Error	Fine Error	Order
L_1	u_0	1.68e-04	3.53e-05	2.25
	u_1	1.68e-04	3.54e-05	2.25
	p	3.15e-03	1.16e-03	1.44
L_2	u_0	2.26e-04	4.63e-05	2.28
	u_1	2.26e-04	4.64e-05	2.28
	p	6.63e-03	2.00e-03	1.72
L_∞	u_0	2.36e-03	5.46e-04	2.11
	u_1	2.36e-03	5.46e-04	2.11
	p	4.12e-02	1.59e-02	1.37

Table 3: Solution error convergence rates for a Newtonian fluid with a vortex initial condition in a rectangle. Data corresponds with Figs. 5 and 6.

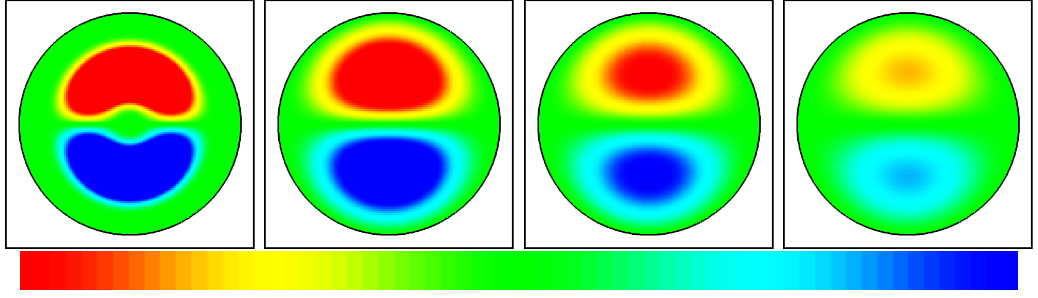


Figure 7: Time-dependent u_0 velocity profiles of a Newtonian fluid with a vortex initial condition in a disk. The domain has 128×128 cells with 2 time step increments using $\Delta t = 3.75 \times 10^{-3}$, -0.25 (red) to 0.25 (blue).

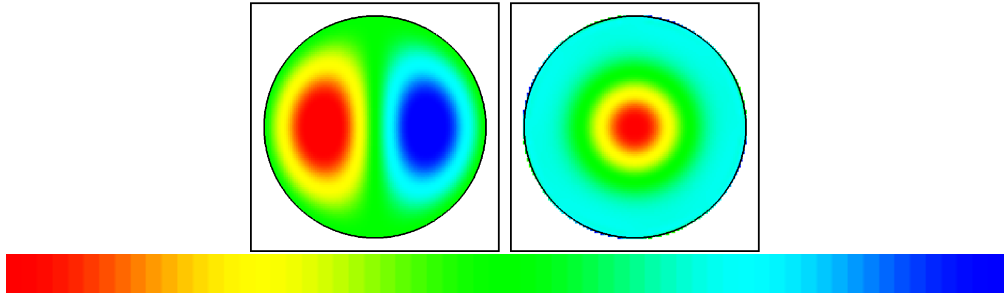


Figure 8: Profiles for a Newtonian fluid in a disk at $t = 2.25 \times 10^{-2}$ (corresponding to the last image in Figure 7.) (Left) u_1 , -0.15 (red) to 0.15 (blue); (Right) hydrostatic pressure p , 0 (red) to 0.032 (blue).

The transverse velocity and pressure corresponding to the final image of normal velocity are shown in Figure 8. The solution error convergence after 20 fine time steps is given in Table 4.

6.3 Hybrid Fluid

For the hybrid fluid, the rheological parameters are $\mu_s = 0.1$, $\mu_p = 0.9$, $\lambda = 1.0$, and $\rho = 1.0$ leading to dimensionless parameters $\text{Re} = 1.0$, $\text{We} = 1.0$, and $\text{Ma} = 1.05$ for the rectangular box geometry. The initial stress is set to zero. The coarse time step is 3.2×10^{-3} for each geometry, corresponding to $\text{CFL} \approx 0.5$. The time-dependent normal velocity is shown in Figure 9. As is the case with the Newtonian fluid, the vortex spreads out and decays over time, with a different shape than the Newtonian case. The transverse velocity, stress, and pressure corresponding to the final image of normal velocity are shown in Figure 10. The solution error convergence after 200 fine time steps is given in Table 5. rheological parameters for the circular geometry, leading to dimensionless parameters $\text{Re} = 0.9$, $\text{We} = 0.9$, and $\text{Ma} = 1.05$. The time-dependent u_0 component of velocity is shown in Figure 11. As with the

norm	Variable	Coarse Error	Fine Error	Order
L_1	u_0	4.06e-04	9.44e-05	2.10
	u_1	4.06e-04	9.44e-05	2.10
	p	5.12e-03	1.58e-04	5.02
L_2	u_0	4.88e-04	1.16e-04	2.07
	u_1	4.88e-04	1.16e-04	2.07
	p	1.04e-02	2.48e-04	5.40
L_∞	u_0	1.06e-03	5.51e-04	0.95
	u_1	1.06e-03	5.51e-04	0.95
	p	7.77e-02	1.13e-03	6.11

Table 4: Solution error convergence rates for a Newtonian fluid with a vortex initial condition in a disk. Data corresponds with Figs. 7 and 8.

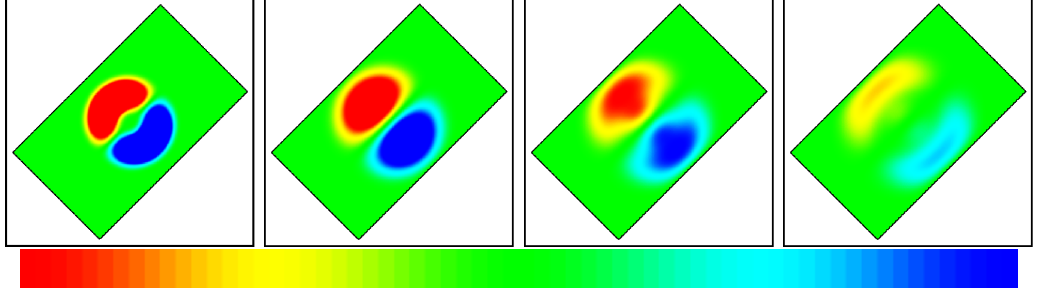


Figure 9: Time-dependent u_n profiles of a hybrid fluid with a vortex initial condition in a rectangle. The domain has 256×256 cells with 30 time step increments using $\Delta t = 1.6 \times 10^{-3}$, -0.25 (red) to 0.25 (blue).

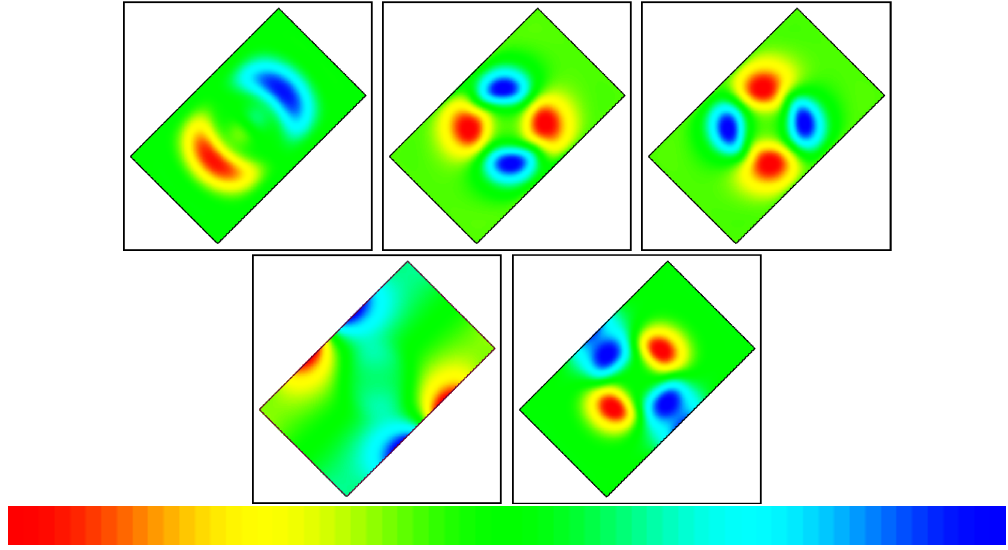


Figure 10: Profiles for a hybrid fluid in a rectangle at $t = 0.144$ (corresponding to the last image in Figure 9.) In order, clockwise from top-left: u_t , -0.15 (red) to 0.15 (blue); normal stress τ_{nn} , -0.25 (red) to 0.37 (blue); normal stress τ_{tt} , -0.25 (red) to 0.37 (blue); shear stress τ_{tn} , -0.30 (red) to 0.29 (blue); hydrostatic pressure p , 0 (red) to 0.55 (blue).

norm	Variable	Coarse Error	Fine Error	Order
L_1	u_0	8.74e-05	2.62e-05	1.74
	u_1	8.99e-05	2.93e-05	1.62
	τ_{00}	1.31e-04	3.78e-05	1.80
	τ_{10}	1.74e-04	5.81e-05	1.58
	τ_{11}	1.33e-04	3.96e-05	1.75
	p	2.49e-04	7.95e-05	1.64
L_2	u_0	1.98e-04	7.53e-05	1.39
	u_1	2.02e-04	7.75e-05	1.39
	τ_{00}	2.47e-04	1.00e-04	1.30
	τ_{10}	3.00e-04	1.28e-04	1.22
	τ_{11}	2.90e-04	1.40e-04	1.05
	p	3.82e-04	1.28e-04	1.58
L_∞	u_0	6.75e-03	3.26e-03	1.05
	u_1	6.82e-03	3.29e-03	1.05
	τ_{00}	2.67e-03	3.45e-03	-0.37
	τ_{10}	8.52e-03	4.40e-03	0.95
	τ_{11}	4.72e-03	6.15e-03	-0.38
	p	6.58e-03	3.16e-03	1.06

Table 5: Solution error convergence rates for a hybrid fluid with a vortex initial condition in a rectangle. Data corresponds to Figs. 9 and 10.

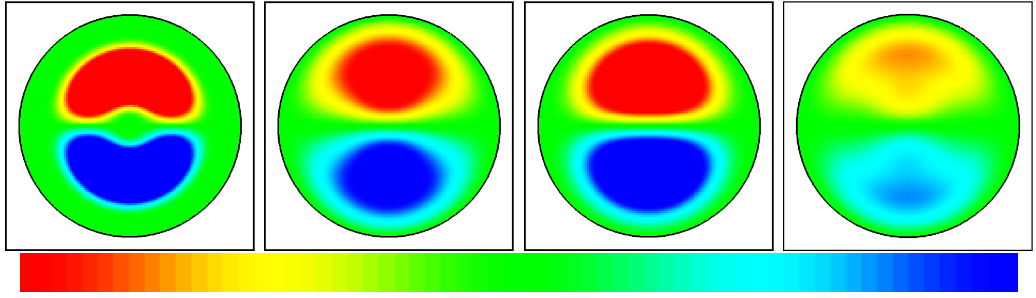


Figure 11: Time-dependent u_0 profiles of a hybrid fluid with a vortex initial condition in a disk. The domain has 128×128 cells with 20 time step increments using $\Delta t = 1.6 \times 10^{-3}$, -0.25 (red) to 0.25 (blue).

rectangular box case, the vortex spreads out to fill the circle and decays over time. The transverse velocity, stress, and pressure corresponding to the final image of u_0 are shown in Figure 12. The solution error convergence after 200 fine time steps is given in Table 6.

7 Conclusions

For each of the test problems, we demonstrate second-order convergence of the solution error in L^1 and first-order in L^∞ for velocity and stress with an advective CFL time step constraint of $\text{CFL} \approx 0.5$, as expected. This is an improvement over [30], in which less than second-order convergence was obtained with a smaller time step, and the algorithm did not support arbitrary smooth geometries. The algorithm also exhibits at least first-order convergence in L^1 for pressure, as expected. In some cases, such as the Maxwell fluid in the rectangular geometry, the convergence rates in L^∞ exceed first-order. This is due to the fact that given the position and shape of the expanded vortex, the largest magnitude errors occur in the interior of the domain, where the algorithm is second-order.

A feature calling for further study is the apparent need for additional projection filters (47) to smooth out the divergence in the velocity field of Maxwell fluids in irregular cells. Approaches include different filtering stencils, or different covered face state extrapolation algorithms.

The first obvious extension to this work is a three-dimensional discretization of the equations. The upwind method [6] and discretizations for Poisson's equation and the heat equation [29] in a three-dimensional embedded boundary framework have already been developed, so the extension is straightforward. The methods in this paper have been developed under the assumption that the geometry is sufficiently smooth. Additional studies are required to determine the robustness of the algorithm in the presence of discontinuous geometries, such as abrupt contractions. This will enable comparisons to standard benchmark problems [1, 26, 27, 30], such as the flow of elastic liquids in hard-cornered planar and axisymmetric contractions.

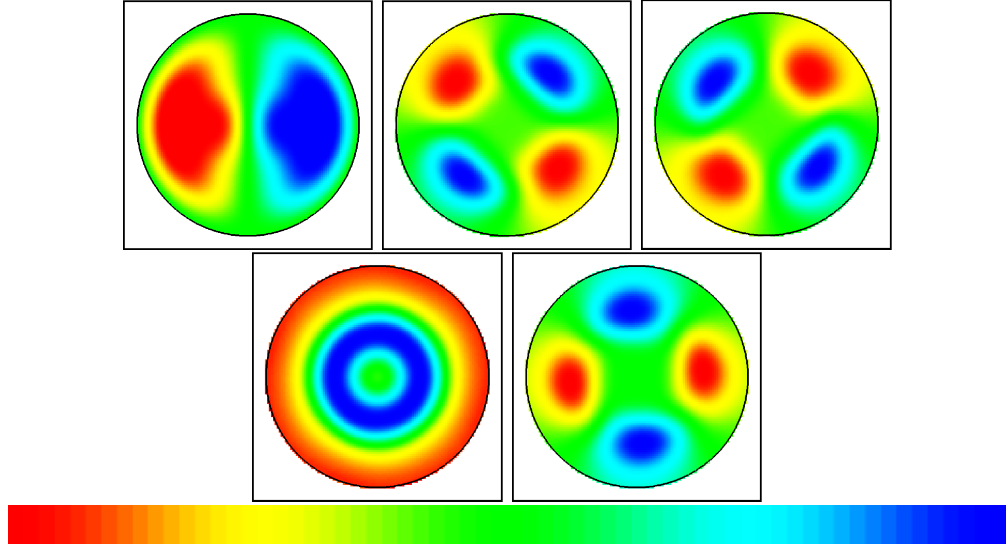


Figure 12: Profiles for a hybrid fluid in a disk at $t = 0.096$ (corresponding to the last image in Figure 11). In order, clockwise from top-left: u_1 , -0.15 (red) to 0.15 (blue); normal stress τ_{00} , -0.25 (red) to 0.35 (blue); normal stress τ_{11} , -0.25 (red) to 0.35 (blue); shear stress τ_{10} , -0.30 (red) to 0.30 (blue); hydrostatic pressure p , 0 (red) to 0.040 (blue).

norm	Variable	Coarse Error	Fine Error	Order
L_1	u_0	1.21e-04	3.05e-05	1.99
	u_1	1.27e-04	3.40e-05	1.91
	τ_{00}	2.66e-04	6.62e-05	2.01
	τ_{10}	3.95e-04	1.25e-04	1.66
	τ_{11}	2.54e-04	6.39e-05	1.99
	p	3.94e-04	1.40e-04	1.50
L_2	u_0	2.23e-04	6.86e-05	1.70
	u_1	2.27e-04	7.12e-05	1.67
	τ_{00}	3.53e-04	9.91e-05	1.83
	τ_{10}	4.94e-04	1.62e-04	1.60
	τ_{11}	3.44e-04	9.73e-05	1.82
	p	4.82e-04	1.72e-04	1.49
L_∞	u_0	2.31e-03	1.15e-03	1.00
	u_1	2.30e-03	1.15e-03	1.00
	τ_{00}	4.47e-03	2.13e-03	1.07
	τ_{10}	3.78e-03	1.64e-03	1.21
	τ_{11}	4.75e-03	2.28e-03	1.06
	p	2.19e-03	1.90e-03	0.20

Table 6: Solution error convergence rates for a hybrid fluid with a vortex initial condition in a disk. Data corresponds with Figs. 11 and 12.

Additional studies are also required to examine the robustness of this algorithm under higher values of We and Ma , and for a variety of operating conditions for experimental comparison [12, 13, 14]. In addition, adaptive numerical algorithms for the incompressible Navier-Stokes equations, in which the grid is locally refined in regions of interest, are being developed [21]. Adaptive techniques have already been used with success for hyperbolic conservation laws [6], so these two methods can be combined to develop a new adaptive projection method for incompressible viscoelasticity. Finally, another possible extension is the discretization of more advanced constitutive models, such as the PTT [25], White-Metzner [35] and Giesekus [11] models. The methods in this paper provide a framework for including the additional terms present in these models.

Acknowledgments

This work was performed under the auspices of the U.S. Department of Energy by the University of California, Lawrence Livermore National Laboratory under contract No. W-7405-Eng-48. Work at the Lawrence Berkeley National Laboratory was supported by the US DOE Mathematical, Information, and Computer Sciences (MICS) Division under contract number DE-AC02-05CH11231. Work at the University of California, Davis was partially supported by the US DOE MICS Division under contract number DE-FG02-03ER25579. A. Nonaka was supported by the Lawrence Livermore National Laboratory through the Student Employee Graduate Research Fellowship Program.

References

- [1] M. A. Alves, P. J. Oliveira, and F. T. Pinho. Benchmark solutions for the flow of Oldroyd-B and PTT fluids in planar contractions. *J. Non-Newtonian Fluid Mech.*, 110:45–75, 2003.
- [2] J. B. Bell, P. Colella, and H. M. Glaz. A second-order projection method for the incompressible Navier-Stokes equations. *J. Comp. Phys.*, 85:257–283, 1989.
- [3] A. J. Chorin. Numerical solutions of the Navier-Stokes equations. *Math. Comp.*, 22:745–762, 1968.
- [4] P. Colella. A direct Eulerian MUSCL scheme for gas dynamics. *J. Sci. Stat. Comput.*, 6:104–117, 1985.
- [5] P. Colella. Multidimensional upwind methods for hyperbolic conservation laws. *J. Comp. Phys.*, 87:171–200, 1990.
- [6] P. Colella, D. T. Graves, B. J. Keen, and D. Modiano. A Cartesian grid embedded boundary method for hyperbolic conservation laws. *J. Comp. Phys.*, 211:347–366, 2006.

- [7] M. J. Crochet, A. R. Davies, and K. Walters. *Numerical Simulation of Non-Newtonian Flow*. Elsevier, New York, 1984.
- [8] R. K. Crockett, P. Colella, R. T. Fisher, R. I. Klein, and C. F. McKee. An unsplit, cell-centered Godunov method for ideal MHD. *J. Comp. Phys.*, 203:422–448, 2005.
- [9] T. A. Gardiner and J. M. Stone. An unsplit Godunov method for ideal MHD via constrained transport. *J. Comp. Phys.*, 205:509–539, 2005.
- [10] J.-M. Ghidaglia and F. Pascal. The normal flux method at the boundary for multidimensional finite volume approximations in CFD. *Eur. J. Mech. B Fluids*, 24:1–17, 2005.
- [11] H. Giesekus. A simple constitutive equation for polymer fluids based on the concept of deformation-dependent tensorial mobility. *J. Non-Newtonian Fluid Mech.*, 11:69–109, 1982.
- [12] S. Gulati. *Effects of Abrupt Changes in Microfluidic Geometry on Complex Biological Fluid Flows*. PhD thesis, University of California, Berkeley, 2007.
- [13] S. Gulati, S. J. Muller, and D. Liepmann. Direct measurements of viscoelastic flows in micro-contractions. In *Proceedings of the 3rd International Conference on Microchannels and Minichannels*, Toronto, Ontario, Canada, June 2005.
- [14] S. Gulati, S. J. Muller, and D. Liepmann. Quantifying viscoelastic behavior of DNA-laden flows in microfluidic systems. In *Proceedings of the 3rd Annual International IEEE EMBS Special Topic Conference on Microtechnologies in Medicine and Biology*, Kahuku, Oahu, HI, May 2005.
- [15] F. H. Harlow and J. E. Welch. Numerical calculation of time-dependent viscous incompressible flow of fluid with free surface. *Physics of Fluids*, 8:12:2182–2189, 1965.
- [16] H. Johansen and P. Colella. A Cartesian grid embedded boundary method for Poisson’s equation on irregular domains. *J. Comp. Phys.*, 147:60–85, 1998.
- [17] D. D. Joseph. *Fluid Dynamics of Viscoelastic Liquids*. Springer-Verlag, New York, 1990.
- [18] D. D. Joseph, M. Renardy, and J.-C. Saut. Hyperbolicity and change of type in the flow of viscoelastic fluids. *Arch. Rat. Mech. Anal.*, 87:213–251, 1985.
- [19] R. Kupferman. Simulation of viscoelastic fluids: Couette-Taylor flow. *J. Comp. Phys.*, 147:22–59, 1998.
- [20] M. F. Lai. *A Projection Method for Reacting Flow in the Zero Mach Number Limit*. PhD thesis, University of California, Berkeley, 1994.

- [21] D. F. Martin, P. Colella, and D. T. Graves. A cell-centered adaptive projection method for the incompressible Navier-Stokes equations in three dimensions. In preparation, 2007.
- [22] P. McCorquodale, P. Colella, and H. Johansen. A Cartesian grid embedded boundary method for the heat equation on irregular domains. *J. Comp. Phys.*, 173:620–635, 2001.
- [23] G. H. Miller and P. Colella. A high-order Eulerian Godunov method for elastic-plastic flow in solids. *J. Comp. Phys.*, 167:131–176, 2001.
- [24] A. J. Nonaka. *A Higher-Order Upwind Method for Viscoelastic Flow*. PhD thesis, University of California, Davis, 2007.
- [25] N. Phan-Thien and R. I. Tanner. A new constitutive equation based derived from network theory. *J. Non-Newtonian Fluid Mech.*, 2:353–365, 1977.
- [26] T. N. Phillips and A. J. Williams. Viscoelastic flow through a planar contraction using a semi-Lagrangian finite volume method. *J. Non-Newtonian Fluid Mech.*, 87:215–246, 1999.
- [27] T. N. Phillips and A. J. Williams. Comparison of creeping and inertial flow of an Oldroyd B fluid through planar and axisymmetric contractions. *J. Non-Newtonian Fluid Mech.*, 108:25–47, 2002.
- [28] J. Saltzman. An unsplit 3D upwind method for hyperbolic conservation laws. *J. Comput. Phys.*, 115:153–168, 1994.
- [29] P. Schwartz, M. Barad, P. Colella, and T. Ligocki. A Cartesian grid embedded boundary method for the heat equation and Poisson’s equation in three dimensions. *J. Comp. Phys.*, 211:531–550, 2006.
- [30] D. Trebotich, P. Colella, and G. H. Miller. A stable and convergent scheme for viscoelastic flow in contraction channels. *J. Comp. Phys.*, 205:315–342, 2005.
- [31] D. P. Trebotich and P. Colella. A projection method for incompressible viscous flow on moving quadrilateral grids. *J. Comp. Phys.*, 166:191–217, 2001.
- [32] E. H. Twizell, A. B. Gumel, and M. A. Arigu. Second-order, l_0 -stable methods for the heat equation with time-dependent boundary conditions. *Adv. Comp. Math.*, 6:333–352, 1996.
- [33] J. S. Ultman and M. M. Denn. Anomalous heat transfer and a wave phenomenon in dilute polymer solutions. *Trans. Soc. Rheology*, 14:307–317, 1970.
- [34] B. van Leer. Towards the ultimate conservative difference scheme. V. A second-order sequel to Godunov’s method. *J. Comp. Phys.*, 32:101–136, 1979.
- [35] J. L. White and A. B. Metzner. Development of constitutive equations for polymeric melts and solutions. *J. Appl. Polymer Sci.*, 7:1867–1889, 1963.

Andrew Nonaka: AJNonaka@lbl.gov
Center for Computational Sciences and Engineering
Lawrence Berkeley National Laboratory, Mail Stop 50A-1148, 1 Cyclotron Road,
Berkeley, CA 94720-8142, USA

David Trebotich: trebotich1@llnl.gov
Center for Applied Scientific Computing
Lawrence Livermore National Laboratory, P.O. Box 808, L-560,
Livermore, CA 94551, USA

Gregory H. Miller: grgmiller@ucdavis.edu
Department of Applied Science
University of California, 1 Shields Ave,
Davis, CA 95616-8254, USA

Daniel T. Graves: dtgraves@lbl.gov
Applied Numerical Algorithms Group
Lawrence Berkeley National Laboratory, Mail Stop 50A-1148, 1 Cyclotron Road,
Berkeley, CA 94720-8142, USA

Phillip Colella: PColella@lbl.gov
Applied Numerical Algorithms Group
Lawrence Berkeley National Laboratory, Mail Stop 50A-1148, 1 Cyclotron Road,
Berkeley, CA 94720-8142, USA